Visible-light-driven water splitting using CdS decorated with nanoparticulate and molecular co-catalysts

Christian M. Wolff[1,2,†], Peter D. Frischmann[3,‡], Marcus Schulze[3], Bernhard J. Bohn[1,2], Robin Wein[1,2], Panajotis Livadas[1,2], Michael T. Carlson[1,2], Frank Jäckel[1,2,§], Jochen Feldmann[1,2], Frank Würthner[3,*], Jacek K. Stolarczyk[1,2,*]

1. Photonics and Optoelectronics Group, Department of Physics and Center for Nanoscience (CeNS), Ludwig-Maximilians-Universität, Amalienstr. 54, 80799 Munich, Germany
2. Nanosystems Initiative Munich (NIM), Schellingstr. 4, 80799 Munich, Germany
3. Institute für Organische Chemie and Center for Nanosystems Chemistry, Universität Würzburg, 97070 Würzburg, Germany

† current address: University of Potsdam, Institute of Physics and Astronomy, Karl-Liebknecht-Straße 24–25, 14476 Potsdam-Golm

‡ current address: Sepion Technologies, 630 Thomas L. Berkley Way #823, Oakland, CA 94612, USA

§ current address: Department of Physics, University of Liverpool, Oxford Street, and Stephenson Institute for Renewable Energy, University of Liverpool, Peach Street, Liverpool L69 7ZF, United Kingdom

* e-mail: wuerthner@uni-wuerzburg.de, jacek.stolarczyk@physik.uni-muenchen.de

Abstract

Full water splitting into hydrogen and oxygen on semiconductor nanocrystals is a challenging task; overpotentials must be overcome for both half-reactions and different catalytic sites are needed to facilitate them. Additionally, efficient charge separation and prevention of back reactions is necessary. Here, we report simultaneous H_2 and O_2 evolution by CdS nanorods decorated with nanoparticulate reduction and molecular oxidation co-catalysts. The process proceeds entirely without sacrificial agents and relies on the nanorod morphology of CdS to spatially separate the reduction and oxidation sites. Hydrogen is generated on Pt nanoparticles grown at the nanorod tips, while Ru(tpy)(bpy)Cl$_2$-based oxidation catalysts are anchored through dithiocarbamate bonds onto the sides of the nanorod. O_2 generation from water was verified by ^{18}O isotope labelling experiments while time-resolved spectroscopic results confirm efficient charge separation and ultrafast electron and hole transfer to the reaction sites. The system demonstrates that combining nanoparticulate and molecular catalysts on anisotropic nanocrystals provides an effective pathway for visible-light driven photocatalytic water splitting.

The urgent need for carbon neutral energy supply to mitigate the anthropogenic climate change drives the quest for alternatives to fossil-fuels.[1,2] Artificial photosynthesis is a promising long-term approach where carefully integrated synthetic components mimic the intricate light-harvesting, charge-separating, and catalytic functions of natural photosynthetic machinery to generate chemical fuels from sunlight and water. [3-6] Multi-electron half-reactions for water oxidation, $H_2O \rightarrow 2H^+ + \frac{1}{2} O_2 + 2e^-$, and reduction, $2H^+ + 2e^- \rightarrow H_2$, have been carefully optimised in isolation where sacrificial reagents serve as an electron or hole scavenger, respectively. [7-10] Despite impressive progress in the development of these essential half-reactions, integrating the two halves into a single functioning device capable of cyclic photocatalytic water splitting under visible illumination remains elusive. Most successful implementations either require UV irradiation, severely limiting the conversion efficiency of the solar spectrum,[11-14] or a two-photon Z-scheme excitation.[15]

Semiconductor nanocrystals (NCs) have been shown to be very effective for hydrogen generation, especially, when combined with either noble metal or molecular catalysts.[16-19] Metal chalcogenide NCs are a particularly promising class, as they combine visible light absorption with good charge transfer properties and appropriate band alignment with the potentials of the relevant redox reactions. For instance, H_2 production with CdS nanorods (NRs) can reach 90% quantum efficiency, when a Pt nanoparticle (NP) is placed at a tip of a nanorod.[20] This arrangement provides good spatial separation between electron transferring to the Pt NP and a short pathway for hole collection in the radial direction.[18] Rapid localisation of the hole in a CdSe dot embedded in the nanorod helps to push the efficiency near the 100% limit,[21] but requires efficient hole extraction mechanism.[22] The reasons are two-fold: a remaining photogenerated hole may recombine with an electron in the co-catalyst, reducing the efficiency;

and a hole can oxidise the lattice sulphide ions or the thiol group of the stabilising ligands, either way damaging the photocatalyst.[23] Oxygen generation from water, relying on multiple hole transfers, usually cannot compete with these detrimental processes, therefore the hole is frequently scavenged directly[24] or indirectly[7] by a sacrificial agent.

Nonetheless, reports suggest that the photosensitised water oxidation with chalcogenide NCs is possible, provided a suitable molecular[25] or nanoparticle[26,27] acceptor is deposited on the nanorod. To this end, Tseng *et al.* described fast hole scavenging (100 ps timescale) from photoexcited CdS nanorods by a co-dissolved ruthenium-based complex, a derivative of $Ru(tpy)(bpy)Cl_2$,[28] followed by 1000-times slower recombination.[29] The hole transfer proceeded even though the molecule was not bound to the nanorods. To drive water oxidation, where four holes must accumulate in the catalyst and the presence of a long-lived charge separated state is critical, substantial improvements are expected by anchoring the catalyst to the semiconductor surface. Although thiol ligands are most commonly used for attaching functional molecules to CdS semiconductors, thiols can be synthetically difficult to work with and are easily oxidised. In contrast to thiols, dithiocarbamates are easily synthesised by mixing carbon disulfide with a secondary alkyl amine in the presence of an additional Lewis base. In addition, dithiocarbamates have a strong chemical and electronic affinity for CdS[30,31] and are more difficult to oxidise than thiols, both valuable characteristics in the context of photo-driven water oxidation.

Here, we report simultaneous H_2 and O_2 evolution by CdS NRs decorated with both a reduction and an oxidation catalyst, in the absence of any sacrificial agents. The approach takes advantage of the anisotropic morphology and charge transfer properties of the nanorods, by placing the electron sink at the tips of the NC and utilising the entire side surfaces for anchoring a $Ru(tpy)(bpy)Cl_2$-based oxidation catalyst.
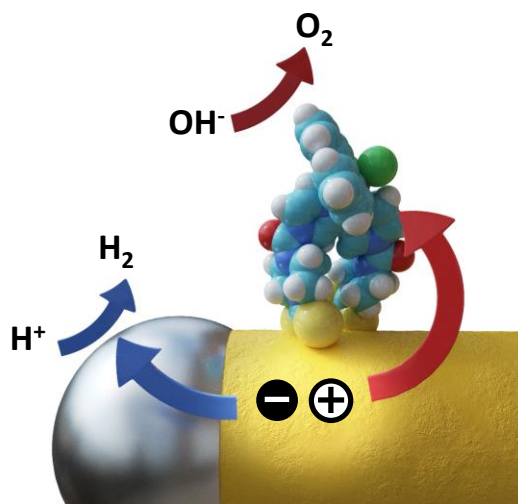
Figure 1. Schematic representation of water splitting on decorated CdS NRs. Photoexcitation of a CdS NR (yellow) provides the driving force for transfer of holes to the molecular catalyst (structure on top). Meanwhile, the CdS NR acts as a conduit to shuttle electrons to the hydrogen evolving Pt nanoparticle (grey) affixed to the NR tip completing the reaction without sacrificial agents.

Preparation of the photocatalyst

The photocatalyst was designed to combine reduction and oxidation co-catalysts at each CdS NR, as illustrated in the Fig. 1. In the first step of the preparation, the CdS NRs were synthesised by high temperature hot injection method, according to a previously published procedure,[32] and redispersed in toluene (Fig. 2a). The transmission electron microscopy (TEM) measurements revealed highly monodisperse nanorods (Fig. 2b), about 95 nm in length and 6 nm in width (*cf*. Supplementary Fig. 1). In the next step, the NRs were decorated with Pt NPs by thermal decomposition of Pt precursor, $Pt(acac)_2$, in a high boiling solvent. The procedure is known to

lead to a selective growth of the metal NPs at the tips of the NRs.[33] Here, the amount of the precursor was adjusted to produce the NPs at both ends, as shown in Fig. 2c and Supplementary Fig. 2. The decorated NRs appear otherwise unaltered from the bare ones, as confirmed by UV-Vis absorption spectra (Fig. 2d) showing no difference in the highly morphology-sensitive excitonic transitions (350, 410, 480 nm). The additional long tail is associated with the *d-sp* transition in Pt and a greater scattering cross-section. On the other hand, the photoluminescence (PL) spectrum (Supplementary Fig. 3) shows, as expected, strong quenching (>95%) of both band edge and trap state emission. This is a sign of a fast electron transfer to the Pt, which strongly hinders radiative recombination. The remaining PL arises from a few non-decorated NRs, in agreement with the statistical analysis of the TEM images (*cf.* Supplementary Fig. 2). Following the decoration, the NRs were transferred into aqueous environment by exchanging the long alkyl chain phosphine-based ligands with cysteine to provide electrostatic stabilisation.
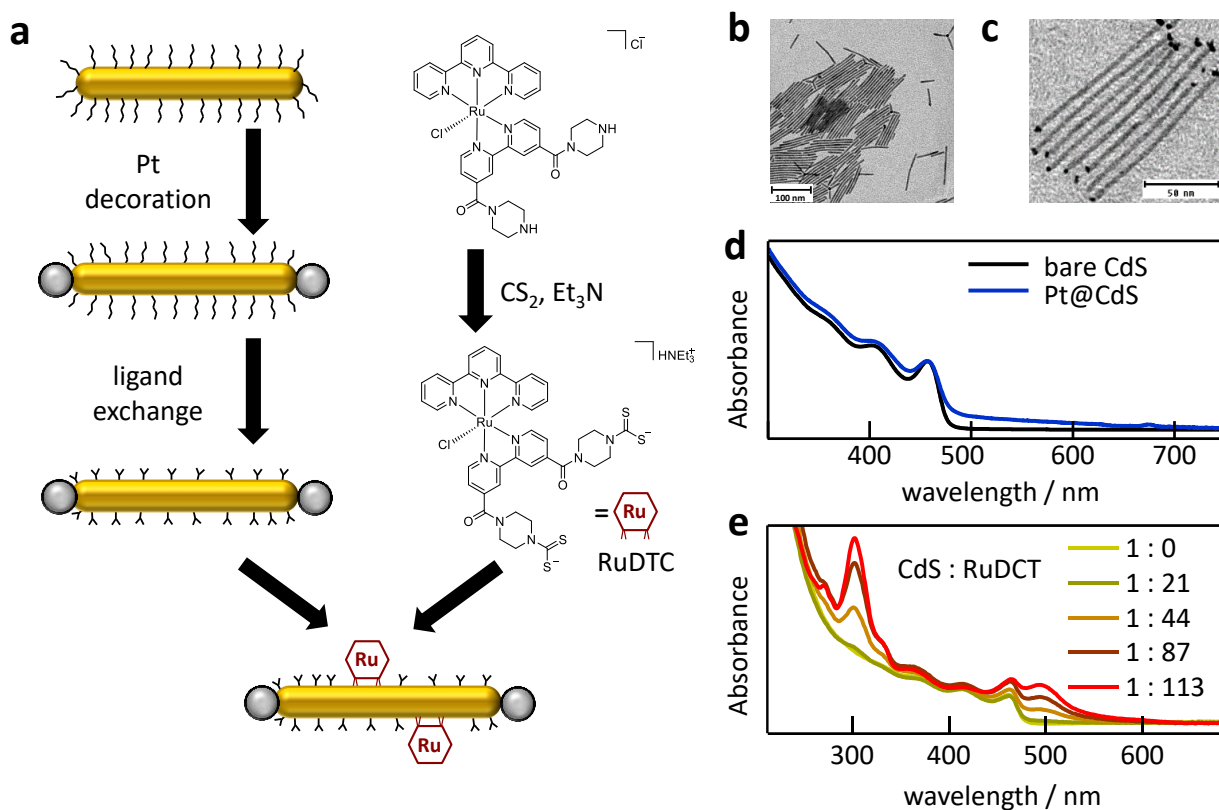
Figure 2. Preparation and characterisation of the photocatalyst. a) Preparation procedure of the Pt-decorated CdS NRs (yellow), through synthesis in organic media, selective growth of Pt NPs (grey) at the tips and phase transfer into aqueous medium with cysteine and anchoring of the Ru(tpy)(bpy)Cl₂ catalyst to the side surfaces of the NRs; b) and c) TEM images of bare and tip-decorated CdS NRs, respectively; d) absorption spectra of the bare and Pt-decorated CdS NRs; e) absorption spectra of CdS NRs functionalised with different amounts of RuDTC, indicated by the CdS NR:RuDTC ratio.

We designed a ruthenium complex (shown in Fig. 2a), which is a derivative of Ru(tpy)(bpy)Cl₂,[28] bearing dithiocarbamate (DTC) groups for chemical ligation to CdS as the water oxidation catalyst. This catalyst was inspired by a related diethyl dicarboxylate derivative that demonstrated rapid hole scavenging (100 ps) from photoexcited CdS, however, only at high

concentrations.[29] The detailed synthetic procedure for RuDTC is given in the Supplementary Methods. To enhance the efficiency of the hole transfer further and separate the holes from the electrons in the Pt NPs, the catalyst was anchored to the surface of the CdS NR. To this end, instead of more common thiols, dithiocarbamates were formed *in situ* at the piperazine units of the ruthenium catalyst prior to adsorption on the CdS surface, as outlined in Fig. 2a. The *in situ* dithiocarbamate bond formation yielding RuDTC was followed in the absence of CdS photosensitiser by ^{1}H NMR spectroscopy where complete conversion to dithiocarbamates was observed after 45 minutes (Supplementary Fig. 4). Electrospray mass spectrometry confirmed the formation of RuDTC with a perfect isotopic distribution observed at *m/z* = 1002 and assigned to the *in situ* formed [RuDTC + Et$_3$NH]$^+$ (see Supplementary Fig. 5). The conversion of CS$_2$ was also monitored by UV-Vis absorption showing a decrease of a characteristic feature at 315 nm with a concurrent increase in the peaks associated with dithiocarbamate at 260 and 290 nm (see Supplementary Fig. 6). To test the attachment of RuDTC to CdS NRs, initially the experiments were performed with bare NRs. The dithiocarbamate linkage was obtained *in situ* by treating the Ru-catalyst precursor with triethylamine and carbon disulfide in the presence of CdS NRs for 20 minutes in water, followed by centrifugation. The absorption spectra of the product (Fig. 2e) are a superposition of CdS and RuDTC features, with an increase in the characteristic absorption of RuDTC at 498 nm used to determine the actual ratio of RuDTC to CdS in the decorated NRs (Supplementary Fig. 7, see details in the Methods section).
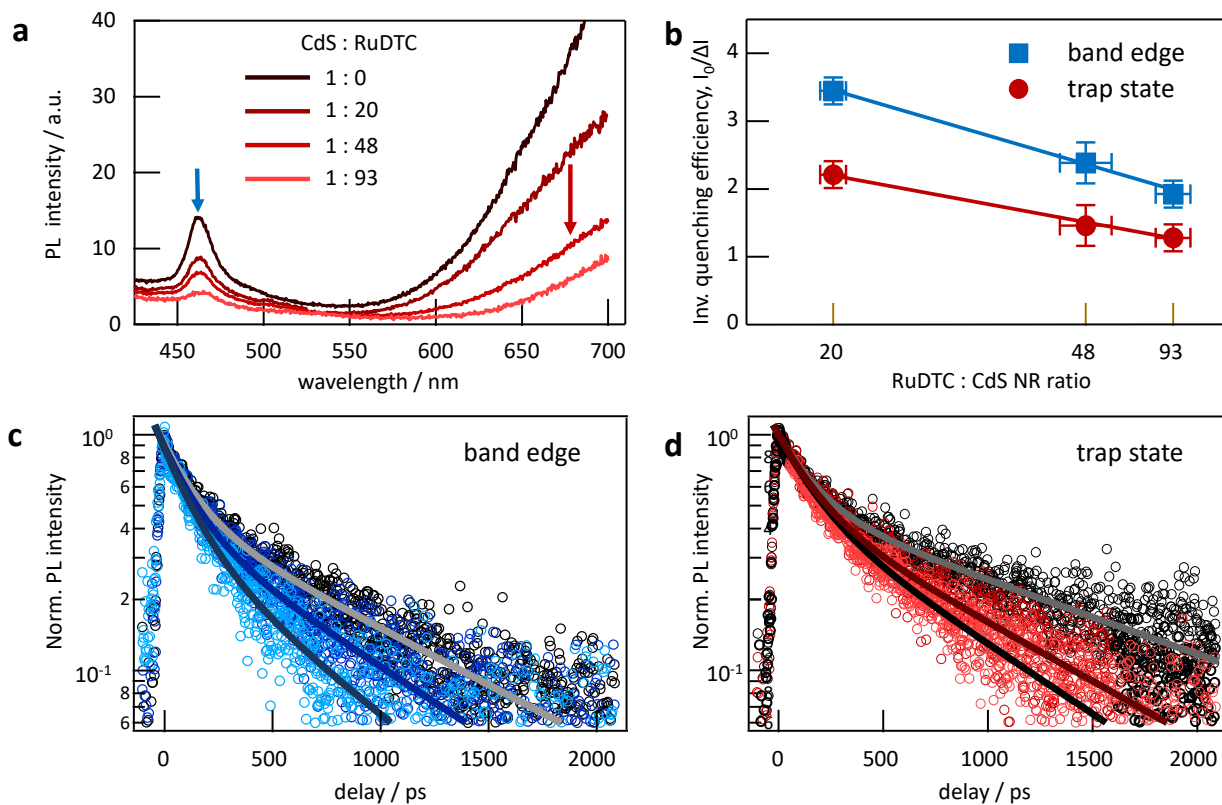
Figure 3. The effect of decoration of CdS with RuDTC on PL quenching and decay dynamics a) PL quenching upon binding of Ru-catalyst for different number of RuDTC molecules per NR. The arrows denote the band edge (blue) and trap state (red) PL; b) Stern-Volmer plot of RuDTC-decorated CdS emission with the extended Langmuir model accounting for attachment of Ru-catalyst on the CdS surface showing the inverse fractional effiency of quenching $I_0/\Delta I$, where I_0 is the PL intensity without RuDTC and ΔI is the change of intensity upon decoration. The error bars correspond to standard deviation of multiple experiments; c) Band edge PL decay plots for Ru-catalyst decorated CdS nanorods with 0 (black), 26 (dark blue) and 53 (light blue) Ru-catalyst molecules per nanorod; d) Trap-state PL decay plots for CdS nanorods decorated with 0 (black), 26 (dark red) and 53 (light red) Ru-catalyst molecules per nanorod. In panels c and d, the solid lines serve as guides to the eye.

Spectroscopic analysis

The PL measurements of the NR decorated with RuDTC reveal that the oxidation catalyst is also a strong quencher for the PL of the NRs, in line with an envisaged hole transfer from CdS to RuDTC. Both band edge and trap state PL under 360 nm excitation decrease (*cf.* Fig. 3a) and the effect is stronger with higher number of catalyst molecules per NR. Förster resonant energy transfer cannot account for the quenching because of very small spectral overlap between emission by CdS and absorption by RuDTC. In this context, a Stern-Volmer model was applied to elucidate the quenching mechanism. The integrated band edge (425–550 nm) and trap state (550–700 nm) PL plotted as a function of RuDTC:CdS ratio (Supplementary Fig. 8) deviates substantially from a linear form, implying that the model of quenching through collisions of two species in solution in not applicable. However, when RuDTC is assumed to form a monolayer on CdS, modelled through a Langmuir adsorption isotherm, a very good agreement with the observed PL quenching is obtained (Fig. 3b, see details in Supplementary Note 1). This corroborates the notion of chemisorption of RuDTC on the surfaces of the CdS NRs.

Time-resolved fluorescence was measured for bare NRs and for NRs decorated with, on average, 26 and 53 molecules of RuDTC per NR to determine the charge transfer dynamics in the system. As shown in Fig. 3c and 3d for band edge and trap state PL, respectively, the lifetimes become shorter with increasing amount of RuDTC. The examination of the decay curves suggests, however, that rates of the decay are similar over the initial 150–200 ps and only differ at longer times. However, the temporal resolution of this experiment does not allow for any insight into the early several picoseconds of the process. Therefore, to investigate the effect of RuDTC further, transient absorption measurements were taken. Colloidal CdS NRs were excited with a

10

100 fs pulse at 400 nm and the differential absorption spectra were acquired with a broad band probe pulse (see Fig. 4a), delayed by up to 2.6 ns. The spectra contain a prominent peak with negative ΔOD (change of optical density) at wavelengths corresponding to the exciton energy in CdS. This bleach feature is attributed in CdS to photoexcited electrons because of the degeneracy of the valence band and higher effective mass of the holes.[34] In addition, the spectra contain a much weaker but broader photoinduced absorption - magnified in amplitude in the inset of Fig. 4a – which is attributed to trapped holes in CdS.[35] Accordingly, this feature rises within 700 fs corresponding to trapping of the holes at surface traps (see Supplementary Fig. 9).[36] This assignment is confirmed by experiments performed in the presence of hole and electron scavengers, respectively. First, the signal virtually disappears in the presence of the hole scavenger sodium sulphite. Second, the signal also rises within 0.7 ps and then stays constant when subjected to the electron scavenger benzoquinone because there is no electron to recombine with. In the absence of any scavengers, the electrons and holes slowly recombine leading to the same rate of decay of both signals, shown in Supplementary Fig. 10.
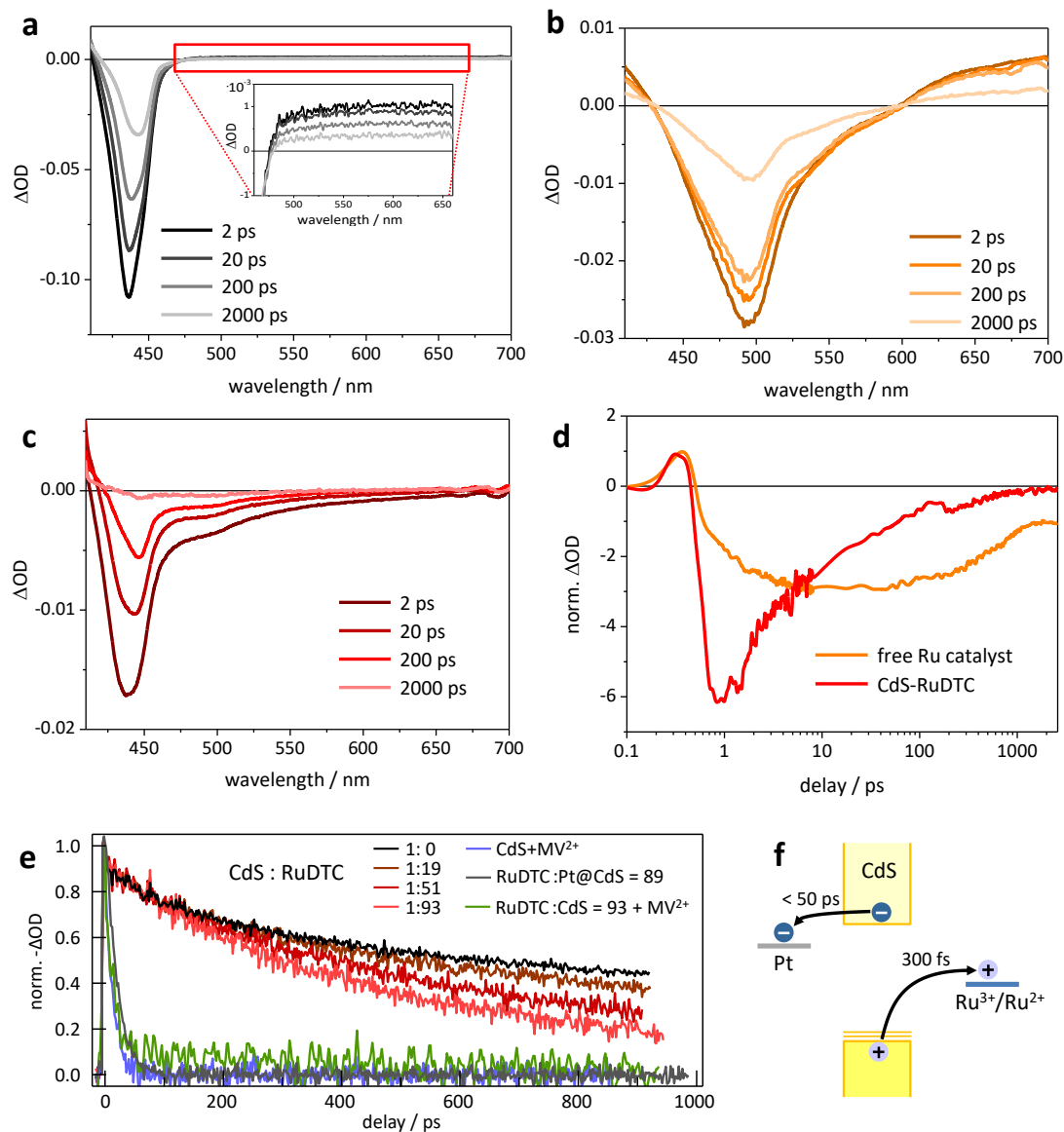
Figure 4. Transient absorption measurements. a) Transient absorption spectra of CdS NRs at indicated delay times measured with 400 nm excitation. Inset shows a magnified view of the 460-660 nm range; b) Transient absorption spectra of the ruthenium catalyst; c) Transient absorption spectra of CdS NR decorated with 82 molecules RuDTC per NR; d) Transient absorption traces for free Ru catalyst and CdS-RuDTC (1:82 ratio) normalised to the first photoinduced absorption peak; e) Relaxation of the CdS band edge bleach in transient absorption of the bare CdS NRs (black) and NRs decorated with RuDTC (red lines), both co-catalysts (dark

grey) or in the presence of an electron scavenger (**MV²⁺**, blue and green); f) schematic illustration of charge transfer processes in the CdS decorated with both Pt and Ru-catalysts.

These results mean that the transient absorption spectra in the region 550-700 nm can provide important insight about the hole dynamics in CdS-based systems, a critical aspect of driving water oxidation reactions. In this context, the transient absorption spectra were acquired for the free ruthenium catalyst (Fig. 4b) and for the CdS NRs decorated with RuDTC (Fig. 4c). The spectra of the former exhibit a bleach of the absorption peak around 500 nm with a tail until 600 nm. The combined system has more complex transient spectra with the bleaching features corresponding to the CdS exciton, the absorption peak of the catalyst and a long tail extending until 650 nm. A closer examination of the trace for the latter system at the relevant region 550-600 nm (Supplementary Fig. 9) reveals a short-lived photoinduced absorption signal followed by a much stronger bleach. This brief positive ΔOD signal appears also in the trace of the free ruthenium catalyst (*cf.* Fig. 4d) implying that this is a feature of the molecule itself. Hence, there is no apparent signal of the CdS trapped hole in the CdS-RuDTC system. For direct comparison, the traces of the free catalyst and CdS-RuDTC were normalised to this feature to simulate having the same amount of the molecular species in both samples. As shown in Fig. 4d, a bleach feature is evident in both traces; however the bleach rises much faster (within 300 fs) and reaches stronger intensity in CdS-RuDTC than in the free catalyst. This means that, in addition to the pump excitation bleaching the molecular transitions of the catalyst, there is an ultrafast component stemming from the hole transfer from the valence band of CdS to the oxidation catalyst. It is in excellent agreement with earlier reports of (sub-)picosecond transfer from Cd chalcogenide nanocrystals to molecular acceptors through dithiocarbamate bonds.[31,37,38] It

compares very favourably with several hundreds of ps needed to transfer holes to the not chemisorbed analogous oxidation catalyst in solution.[29]

On the side of the reduction half-reaction, the CdS exciton bleach decay dynamics corresponds to electron transfer from the CdS NRs. As expected, a slow decay in bare CdS becomes much faster upon addition of an electron scavenger (methyl viologen, **MV^{2+}**), but is not affected by the hole transfer (see Fig. 4e and Supplementary Fig. 11).[20,35] The functionalisation of the NRs with RuDTC has little effect on the decay rate over the first 100 ps, but results in a faster decay afterwards, in line with the time-resolved PL measurements. This increase in the decay rate is stronger with higher density of RuDTC on the surface of CdS. In the presence of Pt NPs or upon addition of **MV^{2+}** the decay is virtually equally fast as for bare rods with **MV^{2+}**. The results confirm that Pt NPs act as electron sinks enabling rapid (less than 50 ps) transfer from CdS, in agreement with earlier observations for Cd chalcogenide nanocrystals.[18] Importantly, this transfer proceeds unperturbed in the presence of RuDTC on the nanorods. Overall, the spectroscopic results point to an efficient charge separation in CdS NRs and transfer of the electrons to Pt NPs and of the holes to RuDTC, as shown in Fig. 4f. Since RuDTC absorbs, albeit weakly, at the pump wavelength (400 nm), an alternative view can also be considered in which the RuDTC units sensitise CdS by injecting electrons to its conduction band. This appears unlikely because it would slow down the bleach decay of the CdS exciton for higher amount of RuDTC on CdS. Not only was this not observed (Fig. 4e), but also pumping the system at 500 nm did not lead to any measurable CdS exciton bleach. Therefore, the full Pt@CdS-RuDTC system operates with CdS as the light absorber and a conduit for charge transfer to Pt and RuDTC for subsequent water reduction and oxidation reactions, respectively.
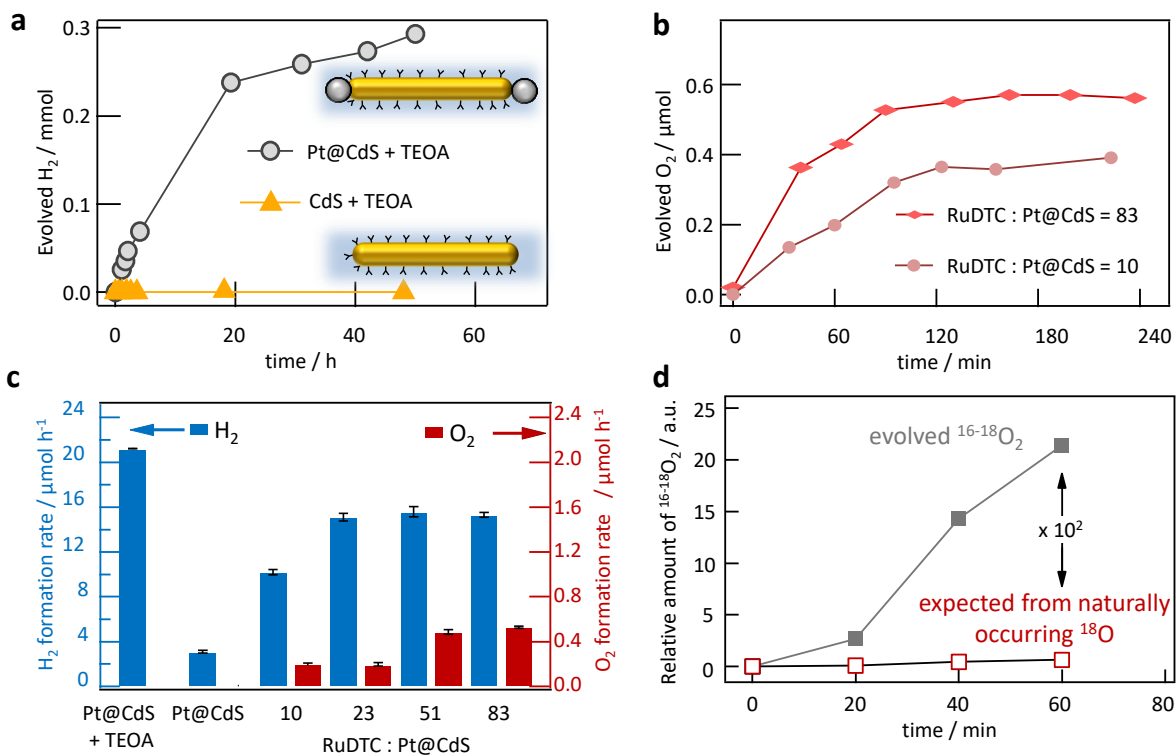
Figure 5. Photocatalytic hydrogen and oxygen generation. a) Hydrogen evolution by bare and tip-decorated CdS NRs; b) oxygen evolution measured for two different CdS-Ru molar ratios; c) comparison of average H_2 and O_2 generation rates over the first hour of illumination, error bars represent the standard deviation of the measured rates. Sacrificial agent (TEOA) was used only in the first experiment (leftmost blue bar); d) comparison of observed evolution of $^{16\text{-}18}O_2$ *vs* expected evolution of $^{16\text{-}18}O_2$ calculated on the basis of natural abundance of ^{18}O isotope from the measured signal for $^{16\text{-}16}O_2$.

Full water splitting

CdS NRs decorated with noble metal co-catalyst NPs are well known for efficient water reduction and hydrogen generation.[18] The architecture with the co-catalyst at the tips of the NR is

15

particularly promising, because it provides long-distance spatial charge separation with an electron transferred to the NPs while the hole remains randomly trapped at the surface of CdS NR. This arrangement has been shown to limit parasitic recombination between the charge carriers.[20] Here, CdS NRs were tested for photocatalytic hydrogen generation under 20 mW·cm^{-2} Xe lamp irradiation, using triethanolamine as a hole scavenger. Near neutral (pH = 6) conditions were chosen to provide a benign environment, compatible also with the oxidation reaction. While the H_2 production by bare CdS NRs is negligible, the CdS-Pt system reached quantum efficiencies of up to 4.9% (see Fig. 5a), confirming that the electron transfer to Pt, as well as subsequent proton reduction, proceed efficiently under these conditions. In separate experiments (see Supplementary Figs. 12 and 13), the oxidation catalyst has been shown in isolation capable of catalysing water oxidation to oxygen using either cerium (IV) ammonium nitrate as a primary oxidant or an electrochemical cell, corroborated further by the redox potentials shown in a Pourbaix diagram (Supplementary Fig. 14).

In the next step, the components of the system were integrated into one photocatalyst, by decorating the CdS NRs first with Pt NPs at the tips and then with the oxidation catalyst. The measurements were performed in mildly acidic conditions (pH = 6) in a custom-built gas-tight quartz cuvette which allowed for automatic sample collection to the gas chromatograph in order to minimise leakage of air into the sample headspace. No sacrificial agents were used. As presented in Fig. 5b, oxygen generation with the rate of 71 μmol/g$_{cat}$·h was detected for 10 molecules of the catalyst per nanorod. The rate increased to 170 μmol/g$_{cat}$·h was detected for 83 molecules per NR. This corresponds to apparent quantum efficiency of 0.10% in the former and 0.27% in latter case. The values already include the adjustment for the small air leakage on the basis of a simultaneous N_2 presence (see Supplementary Fig. 15). Notably, the hydrogen was

also produced by the same samples, with only 25% reduction in formation rate and quantum efficiency in comparison with the Pt@CdS system utilising the hole scavenger (*cf.* Fig. 5c). This suggests an efficient hole removal mechanism in the full system. The rate of oxygen formation increases, as expected, with the number of catalyst molecules anchored to the NRs, although it never reaches stoichiometric results with hydrogen formation (Supplementary Fig. 16). Superoxides or hydrogen peroxide could potentially also form as oxidation or reduction products in the argon atmosphere, but none were detected excluding these possibilities (see Supplementary Fig. 17). It can be therefore inferred that some holes photooxidise the cysteine ligands and the sulphide lattice anions. This is consistent with slow degradation and aggregation of the CdS NR sample, albeit much slower than in the absence of the oxidation catalyst (Supplementary Fig. 18). The limiting factor appears to arise from the pH stability of the thiol-based ligands coating CdS that shows the potential for improvement in O_2 generation using ligands stable across a broader pH range.

Importantly, the oxygen formation by water oxidation was confirmed by isotope labelling. To this end, the reaction was performed in mixture of 10% $H_2^{18}O$ with 90% H_2O and the production of $^{16-18}O_2$ was monitored by a mass spectrometer (see Supplementary Fig. 19). The Figure 5d demonstrates that the strength of the $^{16-18}O_2$ signal exceeds 100-fold the expected signal based just on natural abundance of ^{18}O isotope. Thus, the experiment excludes that air leakage or other adventitious oxygen atoms are the source of the detected O_2.

Conclusion

Photocatalytic water splitting relies on efficiently separating the photogenerated charges, their delivery to the catalytic sites and maintaining the separation long enough for the surface reaction

17

to happen. The inherent anisotropy of the nanorod morphology is particularly well suited for such a process, providing two distinct, easily accessible and spatially separated types of sites at the tips and on the side surface. Our results show that selective attachment of reduction and oxidation catalysts, respectively, at these sites on CdS NRs enables splitting water into hydrogen and oxygen using the blue part of the visible spectrum. The critical aspect is the firm binding of the RuDTC catalyst to the sides of the NRs through dithiocarbamate groups, near the natural hole trapping sites in CdS, but far away from the Pt NPs at the tips. This enables ultrafast (300 fs) hole transfer to RuDTC, three orders of magnitude faster than to free hole acceptors in solution. This not only provides the driving force for water oxidation, but also protects the NRs from degradation by the holes. This demonstrates that integrating anisotropic visible-light absorbing semiconductor NCs with nanoparticle (Pt) and molecular (RuDTC) catalysts opens a viable route for simple, yet effective, water splitting photocatalysts.

Methods

Synthesis of CdS NRs

All reagents were purchased from Sigma-Aldrich. The CdS nanorods were synthesised according to a previously reported hot injection procedure in the presence tetradecylphosphonic acid (TDPA) and trioctylphosphine oxide (TOPO).[32] The NRs were then selectively decorated at the tips with Pt NPs by thermal decomposition of Pt(acac)$_2$ precursor in the presence of oleic acid and oleylamine as stabiliszing ligands using a method published by Habas *et al.*[39]. Both steps proceeded under argon atmosphere. The product was then transferred to aqueous environment by

exchanging the hydrophobic ligands with either mercaptopropionic acid (MPA) or L-cysteine to provide electrostatic stabilisation. This was achieved by precipitating the Pt@CdS with methanol and slow redispersion by vigorous stirring in a mixture of methanol and the hydrophilic ligand. KOH was also added to adjust pH to 10.5 which causes deprotonation of the thiol groups and thereby facilitates binding to cationic Cd^{2+} sites on the NRs. The NRs were then precipitated again and re-dispersed in deionised water. This procedure renders solutions stable over several days (Pt@CdS) to several months (pure CdS). The full details of the procedure are given in the Supplementary Methods.

Synthesis of the Ru catalyst

The details of the synthesis are given in the Supplementary Methods.

Dithiocarbamate bond formation

A dispersion of CdS or Pt@CdS NRs (OD ≈ 1) was mixed with 0−1000 fold excess of Ru-based catalyst, a 3-fold excess of triethylamine (or minimal amounts of 0.01M NaOH) and 1.5-fold excess of CS_2 (both with respect to the catalyst). The mixture was stirred for 5 minutes and then centrifuged 2−3 times (2000 rpm, 5 minutes) with deionised water. The attachment of the Ru-catalyst resulted in minor to strong aggregation (depending on the amount of catalyst per NR) due to ligand displacement and interlinking. In the case of high coverage (> 50 RuDTC molecules per NR) we utilised a milder way to separate unreacted chemicals by centrifuging several times (>2) at 1000 rpm for 1−2 min. with a 50.000 MW filter such that there was still some liquid left.

Determination of RuDTC:CdS ratio in decorated samples

The extinction coefficient of the free Ru-based catalyst was found to be $1.15 \cdot 10^4$ cm$^{-1}\cdot$M^{-1} at the absorption peak at 498 nm (*cf.* Supplementary Fig. 7a) by measuring the OD of its aqueous solution as a function of the concentration (Supplementary Fig. 7b). Separately, the extinction coefficient of CdS NRs was calculated according to Peng *et al.*[40] to be $1.2 \cdot 10^6$ cm$^{-1}\cdot$M^{-1}, at the excitonic peak (460 nm). A linear combination of the absorption spectra, focusing particularly on the excitonic feature of the CdS and the lowest energy absorption feature (~498 nm) of **1**, was then used to fit the spectrum of CdS-RuDTC and calculate the concentration of RuDTC on CdS (*i.e.* average number of molecules per nanorod). An example of this procedure is shown in Supplementary Fig. 7c for the obtained CdS:RuDTC ratio of 1:96 where the ratio of concentrations of the mixed components in the decoration was 1:200. The minor mismatch between fit and measured spectra at shorter wavelengths (~300nm) is due to the formation of dithiocarbamate bonds. In general, the decoration yield was close to 100% for lower intended ratios (less than 20), but decreased significantly for ratios higher than 100 (Supplementary Fig. 7d). This decrease was likely due to a large footprint, steric hindrance and possibly electrostatic repulsion between the RuDTC molecules on the surface of the CdS nanorods.

Transmission Electron Microscopy

Samples were prepared by drop-casting diluted (1:10−1:50) dispersions on a carbon-coated TEM copper grid and air-drying overnight. A JEOL JEM-1011 transmission electron microscope operating at 80kV accelerating voltage was used to acquire the images.

Steady-state and time-resolved absorption and PL spectroscopy

UV-Vis absorption was measured with Cary R 60 UV-Vis or Cary 5000 UV-Vis-NIR by Agilent Technologies, employing an integrating sphere for the latter. PL emission was measured with a

Horiba Jobin Yvon Fluorolog, with the water cooled Horiba R 928 detector at 90° relative to excitation. The samples were excited at 360 nm with 2 nm entrance and 3 nm exit slit width. Transient absorption spectroscopy measurements were carried out using a pump-probe system by Newport, Inc. The short laser pulses (t_{pulse} = 100 fs, f_{rep} = 1 kHz, $\lambda_{central}$ = 800 nm) are generated by a Libra-HE+ Ti:Sapphire amplifier system (Coherent, Inc). A part of each pulse is used to generate the pump pulse via second harmonic generation (λ_{pump} = 400 nm, above the band gap of CdS), which is then focused onto the sample to optically excite charge carriers. The second part of the initial pulse is routed through a delay stage and generates the white light spectrum for the probe pulse in a CaF_2 crystal. Both, the pump and probe beam overlap spatially in the sample and the time delay between the pump and probe pulse is scanned by controlling the stage. The pump intensity was chosen to generate less than 0.1 excitons per NR per pulse to exclude nonlinear optical effects. The OD of the samples was adjusted to ≈ 1 at the band edge of CdS. For CdS band edge bleach dynamics measurements the white light continuum probe pulses were directed through the sample and before passing a bandpass filter at 470 +/− 10 nm onto a lock-in synchronised silicon photodiode as detector, to probe the band edge bleach. In other cases, the spectrally resolved signal was recorded and averaged over a given range to improve the signal-to-noise ratio. Time-resolved PL was measured utilising 400 nm pulses from a second harmonics crystal (BBO) with 800 nm pulses coming from an OPO (Coherent MIRA 900, pumped by a Verdi V10). The generated SH pulses with durations below 10 ps were filtered with a BG40 (Schott GmbH) narrow bandpass filter and excitation was again chosen such that nonlinear effects are excluded (≈ 44 nJ/cm^2 per pulse). The signal was recorded using a streak camera (Hamamatsu C5680).

Mass spectrometry, NMR and FTIR spectroscopy

ESI mass spectra were measured using an ESI micrOTOF Focus from Bruker Daltonics. MALDI-TOF mass spectra were measured using a Bruker Autoflex II spectrometer in reflector mode with a DCTB matrix. ^{1}H NMR spectra were recorded on a Bruker Avance 400 or 600 MHz spectrometer at 293 K. Deuterated solvent was used as the lock and residual non-deuterated solvent as the internal reference (CHCl$_3$ = 7.27 ppm for ^{1}H and 77.00 ppm for ^{13}C; CD$_2$HCN = 1.94 ppm for 1H and 1.39 ppm for ^{13}C; HOD = 4.75 ppm for ^{1}H). FT-IR spectra were measured in the solid state with a Jasco FT-IR-410 infrared spectrometer. Melting points were determined on an Olympus BX41 polarisation microscope and were uncorrected.

Photocatalytic measurements

A xenon lamp was used as an illumination source, together with a water bath and two adjacent long- and short-pass filters to limit the illumination range to 460 ± 50 nm and the intensity to 20 mW/cm^2. Quantitative gas volume measurements were carried out with a GC (Shimadzu-2014) and a purpose-built online setup, which minimises atmospheric contamination. The setup included a ~16 mL custom-built quartz cuvette (see Supplementary Fig. 20), filled with 6 mL of the dispersion of the NRs in deionised water, leaving about 10 mL of headspace. The OD of the samples was adjusted to 1 by dilution (0.5 when the contribution from the RuDTC was subtracted). Aliquots of up to 50µL of this headspace were automatically collected to the GC at prescribed times. The setup was flushed with argon for 10 minutes after each measurement, before resuming the illumination.

Determination of quantum efficiency

The apparent quantum efficiency (QE) of H$_2$ and O$_2$ generation was calculated as a ratio of a number of electrons participating in the product generation divided by a number of photons

incident on the sample over a specified illumination time (1 hour, as in Fig. 5c). To this end, a photon flux was calculated according to equation (1):

$$\Theta = \int_{410}^{510} \frac{I(\lambda)\lambda}{hc} d\lambda \tag{1}$$

where the integral was calculated over the whole filtered spectrum (460 ± 50 nm) . $I(\lambda)$ is the light intensity at wavelength λ determined from the Xe-lamp emission spectrum and a measurement with a ThorLabs 5121C photodiode of total light intensity (20 mW·cm^{-2}), h is Planck constant, c is the speed of light. QE was then calculated according to equation (2):

$$QE = \frac{\alpha \cdot n \cdot N_A}{A \cdot t \cdot \Theta} \tag{2}$$

where α is the number of electrons involved in the formation of one molecule of the product (equal 2 for hydrogen and 4 for oxygen, respectively), n in the number of evolved moles of the product over the illumination time t, N_A is the Avogadro number and A is the illuminated flat surface area of the cuvette.

Isotope labelling

Isotope labelling experiments were carried out in aqueous environment which contained 10% $H_2^{18}O$ water molecules. The measurements were taken with Bruker 456-GC gas chromatograph equipped with a thermal conductivity detector (TCD) and flame ionisation detector (FID) and coupled to a Scion SQ mass spectrometer. The latter was used to monitor the evolution of signals at molecular masses m = 32 (O_2), m = 34 ($^{16\text{-}18}O_2$) and m = 28 (N_2, for estimating the air leakage). The O_2 signal was used to calculate a predicted magnitude of the $^{16\text{-}18}O_2$ signal assuming that its only source was the natural abundance of isotope ^{18}O (0.2%).

Water oxidation with primary oxidant

The free Ru-based catalyst was tested as a water oxidising catalysts using cerium(IV) ammonium nitrate (CAN) as the primary oxidant under strongly acidic conditions. Upon addition of excessive amounts of CAN (concentration = 4 mM, enough to achieve mM concentration of oxygen) to acidic solution, the catalyst shows oxygen evolution for up to 40 minutes. CAN is not stable in solutions with pH>3, due to the formation of insoluble cerium oxide. The oxygen evolution was monitored by a Clark-type electrode (Oxytherm, HansaTech Instruments).

Cyclic voltammetry

Cyclic voltammograms were recorded in solution in a standard three electrode setup with a glassy carbon working electrode, an isolated platinum wire counter electrode and Ag/AgCl reference electrode. All compartments for the measurements were flushed with argon for 20 minutes to avoid signal and interaction by oxygen. All cyclic voltammograms were recorded using a PGSTAT 12 potentiostat (Autolab). The electrodes were purchased from MetrOhm.

Data availability

The data that support the findings of this study are available in the Supplementary Note 2 and from the corresponding authors on reasonable request.

Acknowledgements

Author contributions

All authors contributed to the design of the experiments, the interpretation of the results and a discussion of the outline of the manuscript. C.M.W., P.D.F., M.S., B.J.B., R.W., P.L., M.T.C. carried out the experiments. J.K.S. wrote the manuscript, with input and comments from other authors. J.F., F.W. and J.K.S. supervised the work.

Additional information

Supplementary information is available for this paper.

Correspondence and requests for materials should be addressed to F.W. or J.K.S.

Competing interests

The authors declare no competing interests.

References:

1 Lewis, N. S. Toward Cost-Effective Solar Energy Use. *Science* **315**, 798-801 (2007).

2 Cook, T. R. *et al.* Solar Energy Supply and Storage for the Legacy and Nonlegacy Worlds. *Chem. Rev.* **110**, 6474-6502 (2010).

3   Frischmann, P. D., Mahata, K. & Würthner, F. Powering the future of molecular artificial photosynthesis with light-harvesting metallosupramolecular dye assemblies. *Chem. Soc. Rev.* **42**, 1847-1870 (2013).

4   Tinker, L. L., McDaniel, N. D. & Bernhard, S. Progress towards solar-powered homogeneous water photolysis. *J. Mater. Chem.* **19**, 3328-3337 (2009).

5   Tran, P. D., Artero, V. & Fontecave, M. Water electrolysis and photoelectrolysis on electrodes engineered using biological and bio-inspired molecular systems. *Energy Environ. Sci.* **3**, 727-747 (2010).

6   Osterloh, F. E. Inorganic nanostructures for photoelectrochemical and photocatalytic water splitting. *Chem. Soc. Rev.* **42**, 2294-2320 (2013).

7   Simon, T. *et al.* Redox shuttle mechanism enhances photocatalytic H_2 generation on Ni-decorated CdS nanorods. *Nat. Mater.* **13**, 1013-1018 (2014).

8   Duan, L., Tong, L., Xu, Y. & Sun, L. Visible light-driven water oxidation-from molecular catalysts to photoelectrochemical cells. *Energy Environ. Sci.* **4**, 3296-3313 (2011).

9   Gust, D., Moore, T. A. & Moore, A. L. Solar Fuels via Artificial Photosynthesis. *Acc. Chem. Res.* **42**, 1890-1898 (2009).

10   Hetterscheid, D. G. H. & Reek, J. N. H. Mononuclear Water Oxidation Catalysts. *Angew. Chem. Int. Ed.* **51**, 9740-9747 (2012).

11   Reece, S. Y. *et al.* Wireless Solar Water Splitting Using Silicon-Based Semiconductors and Earth-Abundant Catalysts. *Science* **334**, 645-648 (2011).

12   Gao, Y. *et al.* Visible Light Driven Water Splitting in a Molecular Device with Unprecedentedly High Photocurrent Density. *J. Am. Chem. Soc.* **135**, 4219-4222 (2013).

13   Symes, M. D. & Cronin, L. Decoupling hydrogen and oxygen evolution during electrolytic water splitting using an electron-coupled-proton buffer. *Nat. Chem.* **5**, 403-409 (2013).

14   Wang, X. *et al.* Photocatalytic Overall Water Splitting Promoted by an α–β phase Junction on Ga_2O_3. *Angew. Chem. Int. Ed.* **51**, 13089-13092 (2012).

15   Maeda, K. & Domen, K. Photocatalytic Water Splitting: Recent Progress and Future Challenges. *J. Phys. Chem. Lett.* **1**, 2655-2661 (2010).

16   Han, Z., Qiu, F., Eisenberg, R., Holland, P. L. & Krauss, T. D. Robust Photogeneration of H_2 in Water Using Semiconductor Nanocrystals and a Nickel Catalyst. *Science* **338**, 1321-1324 (2012).

17   Ben-Shahar, Y. *et al.* Optimal metal domain size for photocatalysis with hybrid semiconductor-metal nanorods. *Nat. Commun.* **7**, 10413 (2016).

18   Wu, K. & Lian, T. Quantum Confined Colloidal Nanorod Heterostructures for Solar-to-Fuel Conversion. *Chem. Soc. Rev.* **45**, 3781-3810 (2016).

19   Stolarczyk, J. K., Bhattacharyya, S., Polavarapu, L. & Feldmann, J. Challenges and Prospects in Solar Water Splitting and CO_2 Reduction with Inorganic and Hybrid Nanostructures. *ACS Catal.* **8**, 3602-3635 (2018).

20   Simon, T., Carlson, M. T., Stolarczyk, J. K. & Feldmann, J. Electron Transfer Rate vs Recombination Losses in Photocatalytic H_2 Generation on Pt-Decorated CdS Nanorods. *ACS Energy Lett.* **1**, 1137-1142 (2016).

21   Kalisman, P., Nakibli, Y. & Amirav, L. Perfect Photon-to-Hydrogen Conversion Efficiency. *Nano Lett.* **16**, 1776-1781 (2016).

22   Wu, K. *et al.* Hole Removal Rate Limits Photodriven H_2 Generation Efficiency in CdS-Pt and CdSe/CdS-Pt Semiconductor Nanorod–Metal Tip Heterostructures. *J. Am. Chem. Soc.* **136**, 7708-7716 (2014).

23   Chen, S. & Wang, L.-W. Thermodynamic Oxidation and Reduction Potentials of Photocatalytic Semiconductors in Aqueous Solution. *Chem. Mater.* **24**, 3659-3666 (2012).

24   Berr, M. J. *et al.* Hole scavenger redox potentials determine quantum efficiency and stability of Pt-decorated CdS nanorods for photocatalytic hydrogen generation. *Appl. Phys. Lett.* **100**, 223903 (2012).

25   Ding, T. X., Olshansky, J. H., Leone, S. R. & Alivisatos, A. P. Efficiency of Hole Transfer from Photoexcited Quantum Dots to Covalently Linked Molecular Species. *J. Am. Chem. Soc.* **137**, 2021-2029 (2015).

26   Kalyanasundaram, K., Borgarello, E., Duonghong, D. & Grätzel, M. Cleavage of Water by Visible-Light Irradiation of Colloidal CdS Solutions; Inhibition of Photocorrosion by RuO_2. *Angew. Chem. Int. Ed.* **20**, 987-988 (1981).

27   Kalisman, P., Kauffmann, Y. & Amirav, L. Photochemical oxidation on nanorod photocatalysts. *J. Mater. Chem. A* **3**, 3261-3265 (2015).

28   Concepcion, J. J. *et al.* Making Oxygen with Ruthenium Complexes. *Acc. Chem. Res.* **42**, 1954-1965 (2009).

29   Tseng, H.-W., Wilker, M. B., Damrauer, N. H. & Dukovic, G. Charge Transfer Dynamics between Photoexcited CdS Nanorods and Mononuclear Ru Water-Oxidation Catalysts. *J. Am. Chem. Soc.* **135**, 3383-3386 (2013).

30   Thackeray, J. W., Natan, M. J., Ng, P. & Wrighton, M. S. Interaction of diethyldithiocarbamate with n-type cadmium sulfide and cadmium selenide: efficient photoelectrochemical oxidation to the disulfide and flat-band potential of the semiconductor as a function of adsorbate concentration. *J. Am. Chem. Soc.* **108**, 3570-3577 (1986).

31   La Croix, A. D. *et al.* Design of a Hole Trapping Ligand. *Nano Lett.* **17**, 909-914 (2017).

32   Saunders, A. E., Ghezelbash, A., Sood, P. & Korgel, B. A. Synthesis of High Aspect Ratio Quantum-Size CdS Nanorods and Their Surface-Dependent Photoluminescence. *Langmuir* **24**, 9043-9049 (2008).

33   Mokari, T., Rothenberg, E., Popov, I., Costi, R. & Banin, U. Selective Growth of Metal Tips onto Semiconductor Quantum Rods and Tetrapods. *Science* **304**, 1787-1790 (2004).

34   Klimov, V. I. Optical Nonlinearities and Ultrafast Carrier Dynamics in Semiconductor Nanocrystals. *J. Phys. Chem. B* **104**, 6112-6123 (2000).

35   Wu, K., Zhu, H., Liu, Z., Rodríguez-Córdoba, W. & Lian, T. Ultrafast Charge Separation and Long-Lived Charge Separated State in Photocatalytic CdS–Pt Nanorod Heterostructures. *J. Am. Chem. Soc.* **134**, 10337-10340 (2012).

36   Utterback, J. K. *et al.* Observation of trapped-hole diffusion on the surfaces of CdS nanorods. *Nat. Chem.* **8**, 1061-1066 (2016).

37   Lian, S., Weinberg, D. J., Harris, R. D., Kodaimati, M. S. & Weiss, E. A. Subpicosecond Photoinduced Hole Transfer from a CdS Quantum Dot to a Molecular Acceptor Bound Through an Exciton-Delocalizing Ligand. *ACS Nano* **10**, 6372-6382 (2016).

38   Lee, J. R., Li, W., Cowan, A. J. & Jäckel, F. Hydrophilic, Hole-Delocalizing Ligand Shell to Promote Charge Transfer from Colloidal CdSe Quantum Dots in Water. *J. Phys. Chem. C* **121**, 15160-15168 (2017).

39   Habas, S. E., Yang, P. & Mokari, T. Selective Growth of Metal and Binary Metal Tips on CdS Nanorods. *J. Am. Chem. Soc.* **130**, 3294-3295 (2008).

40   Yu, W. W., Qu, L., Guo, W. & Peng, X. Experimental Determination of the Extinction Coefficient of CdTe, CdSe, and CdS Nanocrystals. *Chem. Mater.* **15**, 2854-2860 (2003).